




Fabrication of liquid metal/diamond hybrid thermal interface materials with high thermal conductivity and low flowability

Wendong Wang^{1,2}, Song Wei³, Xinyu Du⁴, Zifeng Ding⁴, Qingsheng Zhu^{1,2}, Yanxin Qiao⁴, Xiaojing Wang⁴, and Jingdong Guo^{1,2,*} 

¹ School of Materials Science and Engineering, University of Science and Technology of China, Shenyang 110016, China

² Shenyang National Laboratory for Materials Science, Institute of Metal Research, Chinese Academy of Sciences, Shenyang 110016, China

³ Guangxi Key Laboratory of Manufacturing System and Advanced Manufacturing Technology, School of Mechanical and Electrical Engineering, Guilin University of Electronic Technology, Guilin 541004, China

⁴ College of Material Science and Engineering, Jiangsu University of Sciences and Technology, Zhenjiang 212001, China

Received: 7 April 2023

Accepted: 12 June 2023

Published online:

21 June 2023

© The Author(s), under exclusive licence to Springer Science+Business Media, LLC, part of Springer Nature 2023

ABSTRACT

In this work, liquid metal-based hybrid thermal interface materials were fabricated using chromium-coated diamond particles (CCDPs) and eutectic gallium–indium–tin low melting temperature alloy (EGa–In–Sn LMTA), and the changes in material thermal conductivity and viscosity with the volume mixing ratio of liquid metal and diamond were investigated. The thermal conductivity of TIMs shows a bell-shaped trend of first increasing and then decreasing with the increase of CCDP content, reaching the highest value of 126 ± 6 W/m·K at a 50% CCDP volume mixing ratio. When the CCDP content reaches the critical value (40%), the CCDPs formed a chain-like structure connected by LMTA, greatly enhancing heat transfer. The flowability of the LMTA/CCDP composite TIMs shows a decreasing trend with the increase of diamond content. The formation of liquid bridges and the presence of capillary forces cause the TIM to exhibit different flow characteristics from liquid to solid states.

1 Introduction

With the increase in integration and the size reduction of microelectronics chips, the performance of microelectronic devices has been dramatically improved in recent years. Meanwhile, the high integration of microelectronic chips also significantly

improves the power density. Therefore, how to improve the heat dissipation power to a large extent has become one of the most critical chip packaging challenges.

Thermal interface materials (TIMs) can adequately enhance the heat transfer between heterogeneous materials interfaces, which are critical to the overall

Address correspondence to E-mail: jdguo@imr.ac.cn

thermal performance of microelectronic components. In a typical microchip package, as shown in Fig. 1. TIMs were used to reduce the interface thermal resistance and improve heat dissipation from the chip to the heat sink. On the one hand, for interface between two solid surfaces, such as between the chips and the heat sinks, the use of TIMs can significantly improve thermal diffusion. On the other hand, TIMs can fill the micro-gaps that exist on solid surfaces, which has a constructive effect on reducing the interface contact thermal resistance (ICTR) between solid surfaces.

Total thermal resistance between the die and the heat sink includes volume thermal resistance and ICTR, which can be written as:

$$R = R_I + R_{TIM} + R_{II} \quad (1)$$

$$R_{TIM} = \frac{BLT}{\lambda_{TIM}} \quad (2)$$

where R is the total thermal resistance, R_{TIM} is the volume thermal resistance of TIM, R_I and R_{II} are the ICTR on each side of TIM, BLT is the bond line thickness of TIM and λ_{TIM} is the thermal conductivity of TIM.

Several types of TIMs have been developed, including greases [1], gels [2], thermal pads [3], carbon-based TIMs [4], phase change materials (PCMs) [5], solder [6] and low melting temperature alloys [7]. Until now, polymer-based TIMs were still the most widely used commercial TIMs due to their simple and convenient operation. However, their low thermal conductivity greatly limits their application, especially on high-power electronics. Carbon-based materials have high thermal conductivity, but the ICTR is high when they are in contact with heterogeneous materials, which fails to give full play to

their advantages of intrinsic high thermal conductivity. Solder has high thermal conductivity, but requires reflow and surface metallization, which makes it difficult to be used as TIM.

Low melting temperature alloys (LMTAs), also known as liquid metals (LMs) or fusible alloys, have excellent thermal conductivity and good wettability, which make them have great potential in the field of thermal management [8]. Jing [9] proposed using pure liquid metals as thermal interface materials to cool high-performance chips, and prepared a gallium-based liquid metal thermal interface material with thermal resistance of only $5.4 \text{ K}\cdot\text{mm}^2/\text{W}$. Martin and Kessel [10] revealed that the thermal conductivity of liquid metal thermal interfaces can achieve $31 \text{ W}/\text{m}\cdot\text{K}$, while the thermal resistance could be as low as $2 \text{ K}\cdot\text{mm}^2/\text{W}$. Huang et al. [11] propose an improved form of LM/indium film/LM sandwich pad as an efficient thermal interface material, reported a thermal resistance of $3.6 \text{ K}\cdot\text{mm}^2/\text{W}$. Roy et al. [12–14] measured the thermal resistance of 100 Ga, $\text{Ga}_{75.5}\text{In}_{24.5}$, and $\text{In}_{51}\text{Bi}_{32.5}\text{Sn}_{16.5}$ with a matrix-LMTA-matrix structure (the matrix is W, Cu, Ni), an extremely low thermal resistance of $0.5 \text{ K}\cdot\text{mm}^2/\text{W}$ is achieved for $\text{W-In}_{51}\text{Bi}_{32.5}\text{Sn}_{16.5}\text{-W}$ structure.

Coating LMTA on the interface of other TIMs is another effective method to reduce the ICTR. Hill RF and Strader JL [15] obtained TIMs with thermal resistance of $1.7 \text{ K}\cdot\text{mm}^2/\text{W}$ by coating Bi–In–Sn low melting temperature alloy on both sides of nickel-plated copper foil. The advantage is that the amount of liquid metal is small, which limits the overflow of liquid metal as reduces the contact thermal resistance, but the thin layer of liquid metal is easily exhausted due to degradation reaction, resulting in the increase of interface thermal resistance.

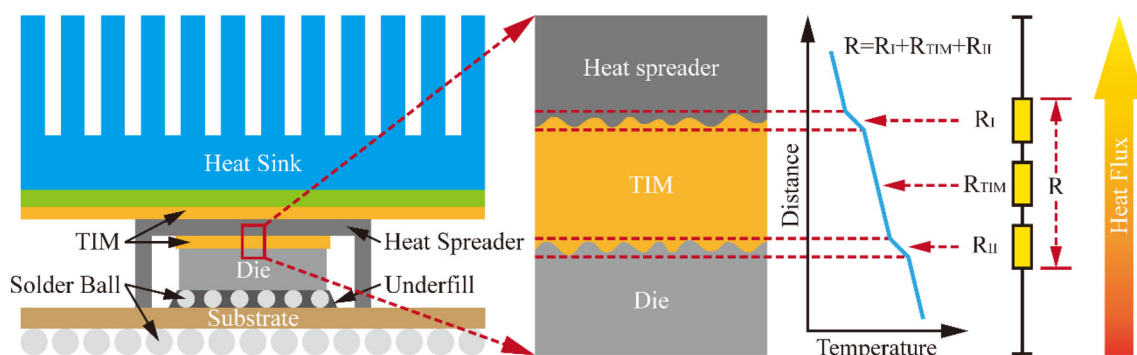


Fig. 1 Schematic diagram showing that an ideal TIM could fill the gap between the die and heat sink and reduce the BTR in a typical microchip package

Coating LMTA on the surface of other TIMs is another effective method to reduce the ICTR. Hill RF and Strader JL [15] obtained a TIM with thermal resistance of $1.7 \text{ K}\cdot\text{mm}^2/\text{W}$ by coating Bi–In–Sn low melting temperature alloy on both sides of nickel-plated copper foil. The advantage is that the amount of liquid metal is small, which limits the overflow of liquid metal while also reduces the contact thermal resistance. However, due to interfacial reactions, the thin layer of liquid metal is easily exhausted, leading to an increase in interfacial thermal resistance.

Adding particles or reinforcements with high thermal conductivity into the matrix is a common method to fabricate TIMs. Research has found that after adding metal particles (such as copper [16–18], silver [19, 20], tungsten [21], gadolinium [22], magnesium [23], nickel [24]) or inorganic high thermal conductivity particles (such as diamond [25–28], aluminum nitride [29], silicon carbide [30], quartz powder [31], boron nitride [32, 33], carbon nanotubes [34, 35], graphene oxide [36] and graphene [37]), the thermal conductivity of liquid metal can be significantly improved. Furthermore, the adding particles to liquid metal can also reduce its flowability, thereby limiting the overflow of liquid metal. However, there were still some problems that need to be clarified. (1) The thermal conductivity does not always increase with the increase of thermally conductive particles, the relationship between thermal conductivity and the content of reinforcements is still unclear. (2) Although the flowability of liquid metals is crucial for their application as TIMs, the relationship between the flowability of the liquid metal and the reinforcements particles content has rarely been reported. (3) The influence of thermal conductive particle distribution on the heat transfer mechanism is still unclear.

Diamond is an ideal thermal conductive filler due to its high thermal conductivity of $2000 \text{ W}/\text{m}\cdot\text{K}$. In our previous work, Wei et al. [25] demonstrated that chromium-coated diamond particles (CCDPs) can significantly increase the thermal conductivity of pure gallium. The chromium layer forms a favorable interfacial bond with diamond, which has a positive effect on improving the phonon mismatch between diamond and liquid metal. The chromium layer also prevents excessive consumption of liquid metal. In this work, EGa–In–Sn LMTA, which has a lower melting point and higher thermal conductivity than Ga, was used as the matrix. Liquid metal-based hybrid thermal interface materials were fabricated by

adding the chromium-coated diamond particles (CCDPs) into the EGa–In–Sn LMTA. The effect of the mixing ratio of liquid metal and diamond on the thermal conductivity and viscosity were investigated. Furthermore, the influence mechanisms on the thermo-rheological properties of the LMTA/diamond composite TIMs are analyzed and discussed intensively.

2 Experimental

The eutectic Ga–In–Sn low melting temperature alloy (EGa–In–Sn LMTA) used in this study was prepared from high-purity materials (Ga, In, Sn: 99.99 wt%). The composition of EGa–In–Sn LMTA is Ga: In: Sn = 67: 20: 13 wt%. According to the order of the melting point from low to high, the raw materials are added to the quartz crucible for melting, and EGa–In–Sn LMTA is obtained after cooling.

Chromium-coated diamond particles (CCDPs, particle size $\approx 40 \mu\text{m}$, HFD-D type, Henan Huanghe Whirlwind Co., China) were prepared by magnetron sputtering method with the base vacuum degree of $5 \times 10^{-3} \text{ Pa}$ at $300 \text{ }^\circ\text{C}$. CCDPs were tested for qualitative analysis using X-ray diffraction (XRD, D8 Advance). The surface morphology and roughness of CCDPs are measured by laser scanning confocal microscope (LSCM, Olympus LEXT OLS4000, Japan). The chromium layer on the diamond surface was analyzed using transmission electron microscopy (TEM; FEI Titan Themis 200, Netherlands). Nitrogen content is the main factor that determines the thermal conductivity of diamonds. The nitrogen impurity content of diamond is detected by oxygen/nitrogen/hydrogen analyzer (LECO TCH-600, America). The melting point of the low melting temperature alloy was measured using differential scanning calorimetry (DSC, Q1000) under an argon atmosphere, scanning from -60 to $60 \text{ }^\circ\text{C}$ and the temperature was ramped at $5 \text{ }^\circ\text{C}/\text{min}$.

To prepare LMTA/particles (CCDPs) composite TIMs, CCDPs were added to EGa–In–Sn LMTA in specific volume ratios (see the Supplementary Information), and then the mixture was stirred in a porcelain mortar until the CCDPs were fully dispersed and mixed, as shown in Fig. 2a.

The thermal conductivity of the TIMs was measured by steady-state thermal methods (ASTM D5470 standard) using a thermal conductivity tester (DRL-

III, Xiangtan Xiangyi Instrument Co., China), as shown in Fig. 2b. The sample was placed between Cu disks, and thermal grease was applied between the test surfaces and the Cu disks to achieve better thermal contact.

The morphology of clad layer was characterized by field emission scanning electron microscope (FE-SEM; Zeiss Supra 55 Sapphire, Germany), and the elements map of the LMTA/particle mixtures was analyzed by X-ray energy dispersive spectroscopy (EDS). The wetting angle between the LMTA and pure chromium plate with ground and polished surface is measured using a contact angle measuring instrument (CAMI, JC2000D).

A mini-slump method was designed to characterize the flowability of LMTA/particles composite TIMs. The testing principle was shown in Fig. 2c. The LMTA/particle mixture was first placed in a cylindrical container, and then the cylindrical container was placed in a cryogenic environment for 30 min to ensure complete solidification of the liquid metal in the mixture. After that, the completely solidified sample was removed from the cylindrical container and was placed in the center of the glass plate. When the solidified sample is completely thawed, the height difference before and after thawing is measured as slump.

Finite element simulation of the heat flux and temperature distribution of the LMTA-particles mixtures was carried out using MATLAB. Thermal conduction follows Fourier's law:

$$q = -\lambda \frac{\partial T}{\partial x} \quad (3)$$

where q is heat flux density, λ is thermal conductivity and T is temperature, the minus sign indicates that heat is transferred in the direction opposite to the temperature gradient.

3 Results and discussion

3.1 DSC of EGa-In-Sn LMTAs

Figure 3 shows the heating DSC curves for EGa-In-Sn LMTA from -60 to 60 °C, with an obvious peak at about 12 °C. Taking the intersection of the tangent of the curve, it can be seen that the solid-liquid transition temperature is about 11 °C. Since the EGa-In-Sn LMTA is a ternary eutectic alloy, a ternary eutectic reaction $L = (\text{Ga}) + \text{In}_3\text{Sn} + (\text{Sn})$ occurs at this solid-liquid transition temperature (see Fig. S2 in the Supplementary Information).

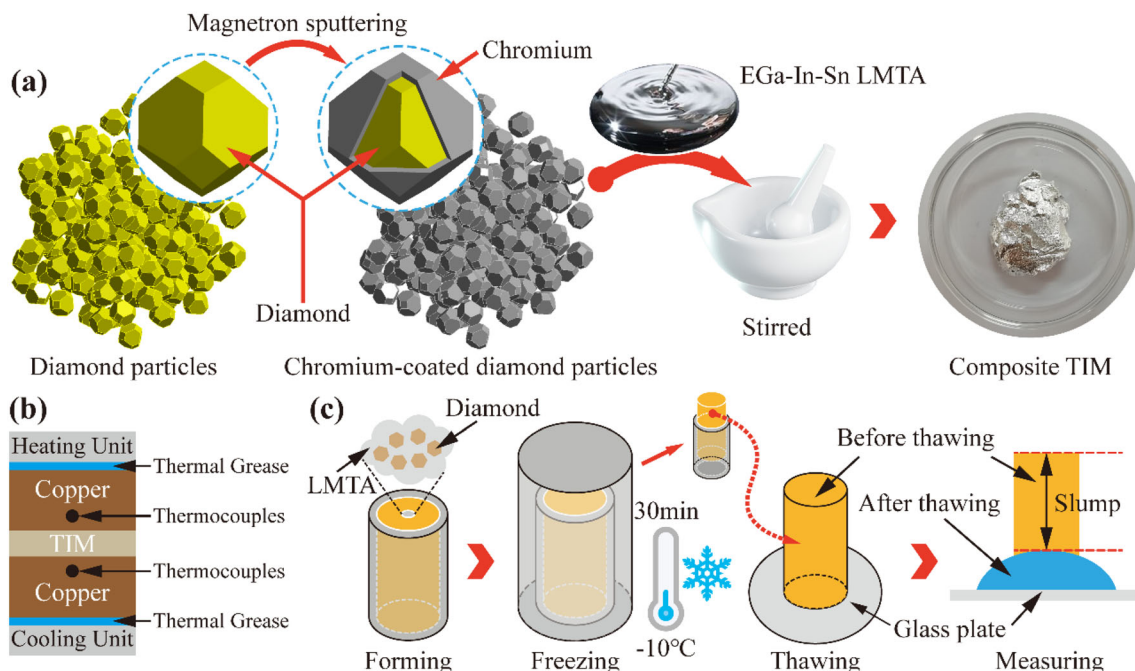


Fig. 2 **a** Schematic diagram of the procedure to fabricate LMTA/particles composite TIMs; **b** Schematic of a typical ASTM D5470 standard setup; **c** Schematic diagram of mini-slump method test principle

3.2 Microstructure of CCDPs

Scanning electron microscopy (SEM) secondary-electron imaging (SE2) characterization and X-ray energy dispersive spectrometer (EDS) map analyses of the pure diamond particles and the CCDPs are displayed in Fig. 4a–e. The pure diamond particles are dark in color, and have a complete polyhedral shape, as shown in Fig. 4a. The surface of pure diamonds is smooth and reflective because pure diamonds are transparent and have a certain reflection effect on light. While for the CCDPs, EDS analyses show that the chromium coating completely envelops the diamond, as shown in Fig. 4b, d and e. Compared with pure diamond, CCDP is off-white in color and has a rougher surface.

Figure 4f shows the XRD patterns of CCDPs and pure diamond particles. The diffraction peaks at $2\theta = 43.9^\circ, 75.3^\circ$ and 91.5° correspond to the diffractions from (111), (220) and (311) planes of diamond (PDF#06-0675), respectively, and the diffraction peaks observed at $2\theta = 44.4^\circ, 64.6^\circ, 81.7^\circ$ and 98.1° correspond to the diffractions from (110), (200), (211) and (220) planes of chromium (PDF#06-0694), respectively. Since the chromium layer coated on the surface of the diamond is only about 10 nm (Fig. 4g) the diffraction peaks of chromium are much weaker than that of diamond particles. In our previous research, the formation of very thin carbide Cr_xC_y layers in the interface between diamond particles and

chromium layers was confirmed by the HRTEM image and corresponding FFT pattern [25].

The thermal conductivity of diamond is affected by many factors, such as crystal type, grain size, impurity content and so on. Among them, the nitrogen content is the main factor that determines the thermal conductivity of synthetic Ib-type diamonds. At room temperature, the thermal conductivity of diamond and its nitrogen content satisfy a linear relationship shown in Fig. 4h [38]:

$$\lambda_{\text{Diamond}} = 2200 - 3.27C_N \quad (4)$$

Where λ_{Diamond} is the thermal conductivity of diamond, C_N is the nitrogen content of diamond. The nitrogen content of diamond particles is 190 ppm as measured by the TCH-600 oxygen/nitrogen/hydrogen analyzer. According to formula (4), the thermal conductivity of the diamond used in this experiment is 1578.7 W/m·K.

3.3 Microstructures of LMTA/CCDPs composite TIMs

Figure 5a–j show the SEM characterization of LMTA/CCDP composite TIMs, indicating that the wettability of chromium coating with LMTA is quite good, which may dramatically improve the phonon mismatch between diamond and LMTA. The morphology of the LMTA/CCDPs composite TIMs is highly dependent on the mixing volume ratio of CCDPs. When the TIMs contain less than 50% CCDPs, CCDPs were immersed in LMTA and uniformly dispersed. However, as the CCDP content exceeds 60%, the state of CCDPs in the LMTA gradually changes from complete immersion to liquid bridge connection. This liquid bridge connection method leads to insufficient filling of the space between CCDPs.

In addition, even if the proportion of liquid metal is only 15%, LMTA can also wrap the CCDPs well, as shown in Fig. 5j, which means that there is good wettability between LMTA and CCDPs. Interestingly, the wetting angle between the LMTA and pure chromium plate was measured to be 131.5 degrees, as shown in Fig. 5k, which indicates that the LMTA and chromium are not wetting. It has been reported that gallium oxide attached to the surface of W particles can enhance the wettability between Gallium and W particles [21]. As a gallium-based alloy, EGa–In–Sn LMTA also tends to form an oxide film on the

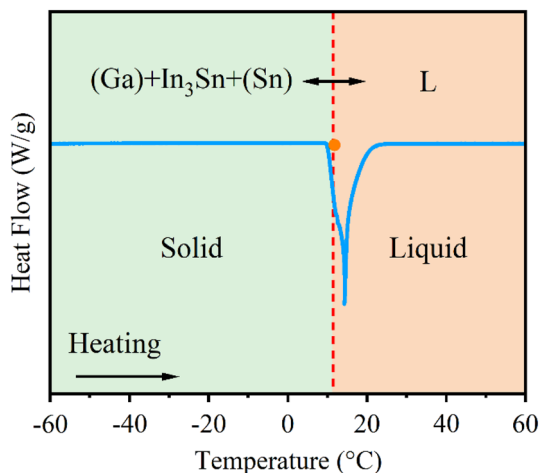


Fig. 3 Heating DSC curve for EGa–In–Sn LMTAs from – 60 to 60 °C

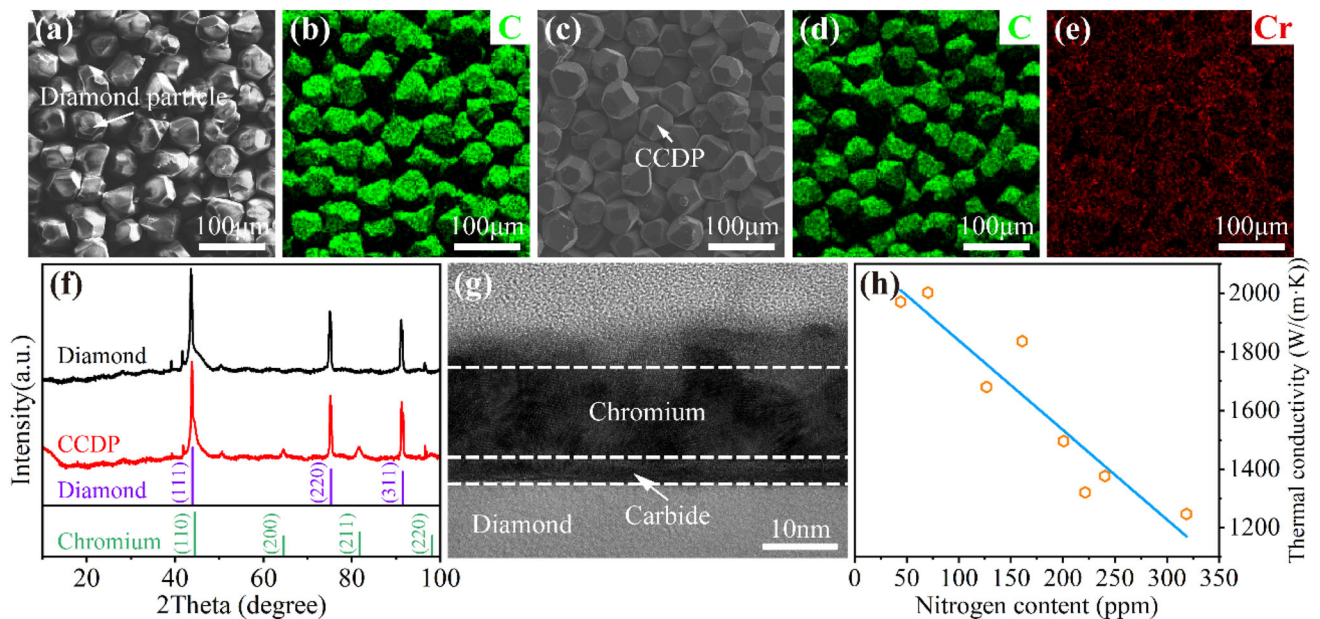


Fig. 4 Scanning electron microscopy (SEM), X-ray energy dispersive spectrometer (EDS), and X-ray diffraction (XRD) characterization of the CCDPs and the pure diamond particles. **a** and **b** SEM and EDS of the pure diamond particles; **c**, **d** and

e SEM and EDS of the CCDPs; **f** XRD characterization of the CCDPs and pure diamond particles; **g** Cross-sectional TEM bright-field image of the interfacial layered structure; **h** Relation between diamond thermal conductivity and its nitrogen content

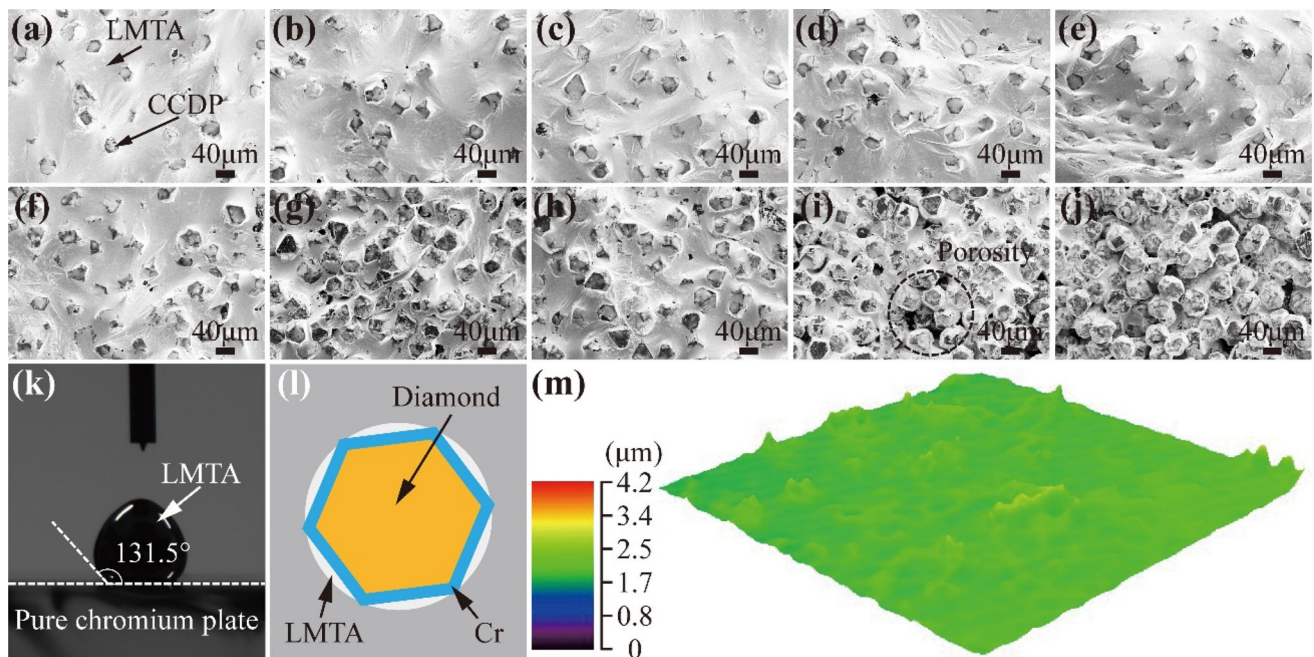


Fig. 5 **a–j** SEM characterization of LMTA/CCDPs composite TIMs with different LMTA: CCDPs: **a** 90:10; **b** 80:20; **c** 70:30; **d** 60:40; **e** 50:50; **f** 40:60; **g** 30:70; **h** 25:75; **i** 20:80; **j** 15:85;

k Wetting angle of LMTA and pure chromium plate; **l** Schematic diagram of LMTA and CCDP wetting; **m** Surface morphology of CCDP

surface. During the mixing and stirring process, the oxide film may be broken and adhere to the surface of CCDPs, enhancing the wettability between LMTA

and CCDPs. Furthermore, the undulating chromium coating on the diamond surface may also aid in the adhesion process (Fig. 5m).

3.4 Thermal conductivity

Figure 6a and b show the thermal conductivity and interface thermal conductivity (ITC) of the LMTA/CCDP composite TIMs versus CCDP mixing volume ratio. With the increase of the CCDP mixing volume ratio, the thermal conductivity of LMTA/CCDP composite TIMs first increases and then decreases, showing a bell-shaped trend. When the volume ratio of LMTA and CCDPs is 1:1, the thermal conductivity of the LMTA/CCDP composite TIMs reaches a peak of 126 ± 6 W/m·K, which is 4.35 times the thermal conductivity of LMTA (Fig. 6a). Interestingly, the curve rises sharply when the CCDP mixing volume ratio reaches 40%. Meanwhile, compared to commercial TIMs (Fig. 6c), the wide range thermal conductivity of LMTA/CCDP composite TIMs can adapt to more use environments. And compared to gallium/chromium-coated diamond composites [25], the LMTA/CCDP composite TIMs still has advantage in thermal conductivity (126 ± 6 W/m·K for LMTA/CCDP composite at a 50% CCDP volume mixing ratio and 112.5 W/m·K for Ga/CCDP

composite at a 47% CCDP volume mixing ratio). This indicates that chromium-coated diamond is very effective in enhancing the thermal conductivity of gallium-based liquid metals.

The thermal conductivity of LMTA/CCDP composite TIMs mainly depends on the thermal conductivity of the diamond, the thermal conductivity of LMTA and the interface thermal conductivity (ITC) between diamond and LMTA. Because the thermal conductivity of diamond and LMTA is known, the only unknown parameter is the ITC. According to the different effective medium (DEM) model, the ITC between LMTA and CCDP can be calculated by [39]:

$$[1 - \Phi] = \frac{a\lambda_{ITC}(\lambda_C - \lambda_D) + \lambda_D\lambda_C}{a\lambda_{ITC}(\lambda_M - \lambda_D) + \lambda_D\lambda_M} \left[\frac{\lambda_M}{\lambda_C} \right]^{\frac{1}{3}} \quad (5)$$

Where λ_C , λ_D , and λ_M refer to the thermal conductivity of LMTA/CCDP composite TIMs, CCDP and LMTA, respectively. a is the radius of CCDPs. Φ is the volume fraction of CCDPs. And λ_{ITC} is interfacial thermal conductivity. The parameters in the application are summarized in Table 1.

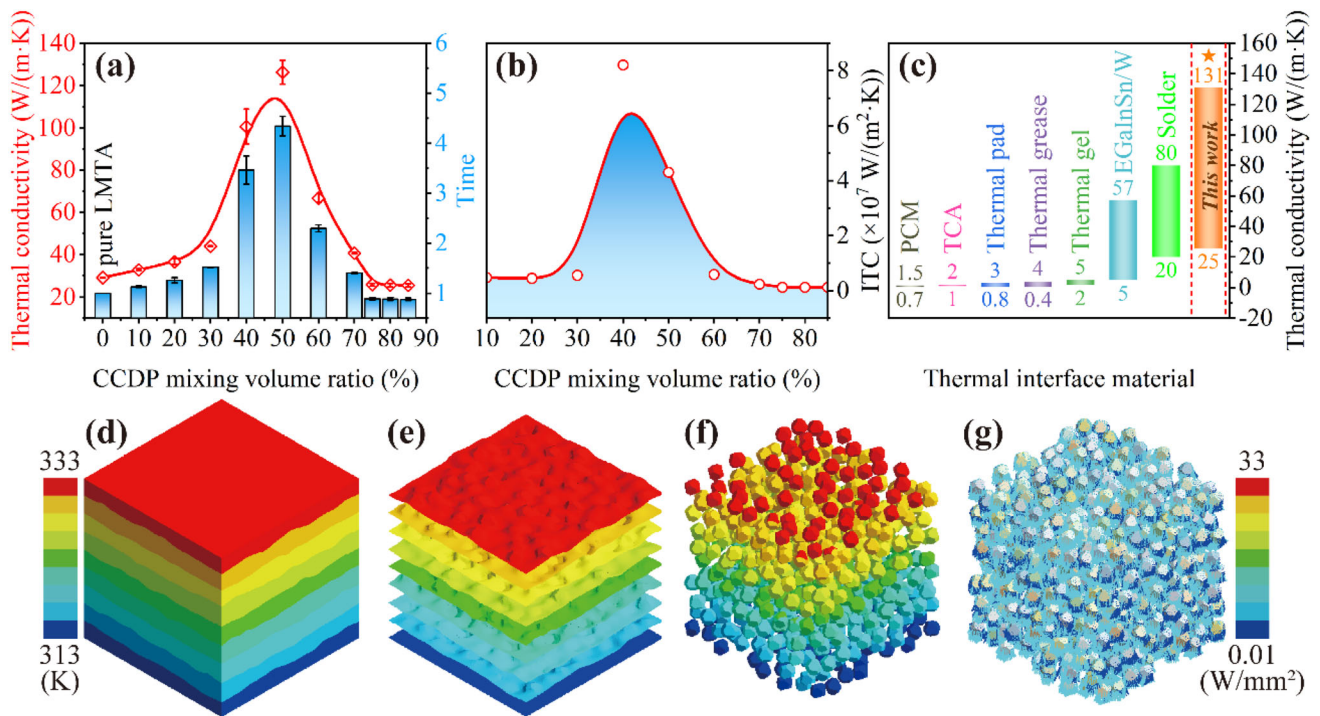


Fig. 6 a Thermal conductivity of LMTA/CCDP composite TIMs and its increasing times relative to LMTA at different volume mixing ratios; b ITC between diamond and LMTA calculated by DEM model; c Comparison of thermal conductivity between commercial TIMs and this work; d–g Finite element analysis

calculation results of LMTA/CCDP composite TIMs when the volume mixing ratio of LMTA: particles are 50:50; d and e Temperature gradient; f Temperature gradient of CCDPs; g Heat flux vector plot of CCDPs.

By substituting all the parameters into the DEM model, the ITC value between LMTA and CCDPs can be calculated, as shown in Fig. 6b. The ITC values remain almost unchanged when the CCDP mixing volume ratio is increased from 10 to 30%. However, when the CCDP contents reach 40%, the ITC value sharply increases. The ITC between LMTA and CCDPs is mainly determined by the coverage and wetting of LMTA on CCDPs. When the CCDP contents is 30 and 40%, there is no significant difference in the coverage and wettability of LMTA on the diamond surface, so the sharply increase of the ITC is unreasonable.

In the DEM model, the particles were assumed to be uniformly dispersed in the matrix. In this geometry, the thermal conductivity of the composite depends on the particle size of the dispersed phase if boundary resistance is high. While for high particles concentrations, Every et al. [38] proposed an approach along the lines of Bruggeman effective medium theory, which proceeds from the premise that the fields of neighboring particles can be taken into account by adding the dispersed particles incrementally, taking the surrounding medium to be the existing composite at each stage. This model is in good agreement with the experimental results when the CCDPs are less than 30%, but when the CCDPs contents reach 40%, the distance between diamond particles is very close, the DEM model may not be applicable for this situation.

To clarify the heat transfer mechanism of LMTA/CCDP composite at high particle concentration, finite element analysis was introduced, and a LMTA:CCDPs volume mixing ratio of 50:50 was selected as the object. According to the temperature gradient distribution nephogram shown in Fig. 6d and e, the temperature distribution inside the LMTA/CCDP composite TIMs is uniform. The isotherms of LMTA/CCDP composite TIMs tend to distribute along the CCDP contour because of the extremely high thermal conductivity of the CCDP. After hiding the LMTA matrix (Fig. 6f and g), it can be found that the CCDPs are uniformly distributed inside the LMTA, and the

temperature decreases uniformly with the direction of heat flow. The CCDPs form a three-dimensional network chain structure inside the LMTA matrix, which is the main channel to undertake the heat flow (see Fig. S3 in the Supplementary Information).

The distance between CCDPs in LMTA has a significant impact on the thermal transfer performance of the LMTA/CCDP composite TIMs. To more clearly reflect the influence of the distance between CCDPs, the pitch-to-diameter ratio is defined as the ratio of the distance between CCDP surfaces to CCDP diameter:

$$\xi = \frac{d}{R} \quad (6)$$

where ξ is the pitch-to-diameter ratio, d is the distance between CCDP surfaces, R is the CCDP diameter, as shown in Fig. 7a.

The finite element models for the different pitch-to-diameter ratios are shown in Fig. 7b, and the FEM calculated results are shown in Fig. 7c and d. It can be seen from these curves that ξ has a very significant impact on temperature gradient and heat flux density.

The heat flux between particles decreases with increasing ξ . When $\xi < 0.2$, the heat flux density sharply increased, indicating that the three-dimensional network chain structure began to play a major role (Fig. 7d). The maximum heat flux appears at $\xi = 0$, indicating that the heat transfer efficiency is highest when the thermally conductive particles are in closely contact.

Treat CCDP as a spherical, the ξ of LMTA/CCDP composite TIMs with different CCDP contents were calculated, as shown in Fig. 7e. When the CCDP content reaches 40%, ξ is about 0.22, and when the CCDP content reaches 50%, ξ is about 0.13. Considering that the shape of the CCDP is irregular, the actual ξ will be much smaller. According to Fig. 7d, the heat flux dramatically increases when $\xi < 0.2$. Therefore, when the CCDP content reaches 40%, the CCDPs were close enough to form a chain-like structure connected by a thin layer of LMTA, which greatly enhanced the heat transfer. When the CCDP content reaches 50%, ξ continues to decrease, but pores emerge due to insufficient LMTA filling, so although the thermal conductivity still increased, the rate is slower due to the presence of pores. When the CCDP contents exceeds 60%, the pores increased and

Table 1 The parameters associated with adhesive ITC

λ_D (W/(m·K))	λ_M (W/(m·K))	Φ (vol%)	a (μm)
1578.7	29.1	10–85	20

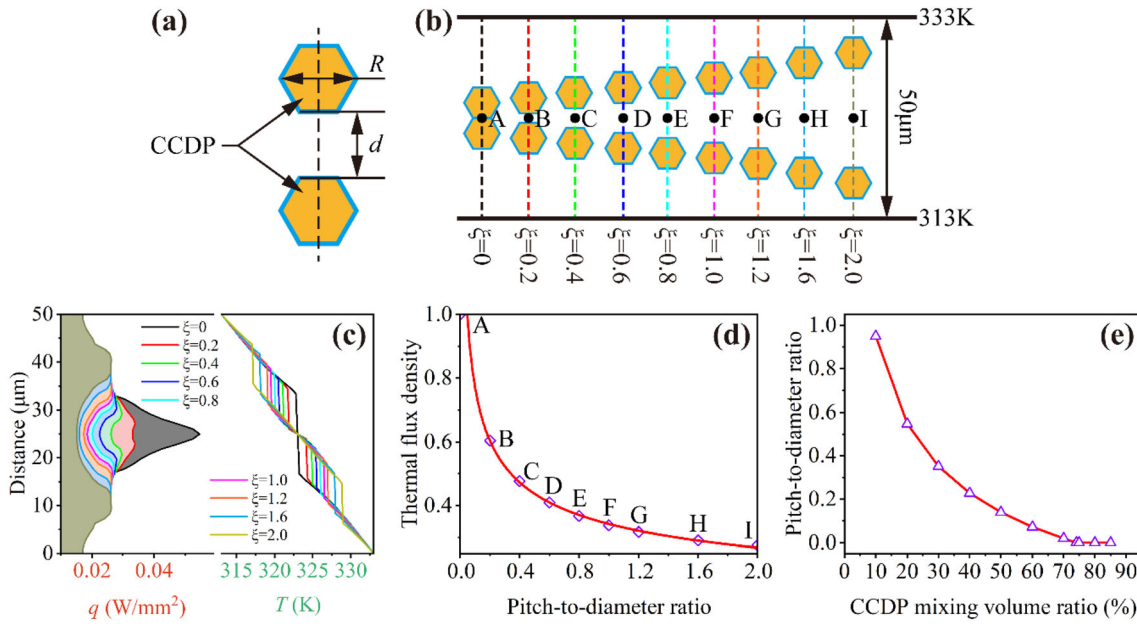


Fig. 7 **a** Schematic diagram of pitch-to-diameter ratio; **b** Schematic diagram of finite element analysis with different pitch-to-diameter ratio; **c** Results of finite element analysis of temperature gradient (T) and heat flux density (q) with different

pitch-to-diameter ratio; **d** Relationship between heat flux density at the center point and pitch-to-diameter ratio in **b**; **e** Relationship between CCDP mixing volume ratio and pitch-to-diameter ratio

connected to form another three-dimensional network chain structure dominated by air, resulting in a sharp decrease in the thermal conductivity of the LMTA/CCDP composite TIM.

3.5 Flowability

Flowability is a key parameter for the application of LMTA-based TIMs. A mini-slump method was used to characterize the flowability of LMTA/particles composite TIMs. In this method, the deformation of LMTA/CCDP composite TIMs is mainly caused by self-weight stress, as shown in Fig. 7a. Regarding the LMTA/CCDP composite TIMs as plastic fluid conforming to the Bingham model, and using yield stress and viscosity to characterize the rheological properties of LMTA/CCDP composite TIMs, there are:

$$\sigma = \sigma_0 + \eta\gamma \tag{7}$$

Where σ is stress, σ_0 is yield stress, η is the viscosity, and γ is the shear rate.

The yield stress σ_0 can be determined based on the slump S . According to Fig. 8a, the stress at any horizontal position of the original height is:

$$\sigma = \frac{\rho g V}{\pi r^2} \tag{8}$$

Where ρ is the density of the LMTA/CCDPs mixtures, as shown in Table 1, $g = 9.8 \text{ m/s}^2$ is gravitational acceleration, r is the radius of the cylinder, V is partial volume above horizontal position, which can be written as:

$$V = \frac{2}{3} \pi r^3 + (z - r) \pi r^2 \tag{9}$$

Where z is the distance from the horizontal position to the top. Therefore, the stress at any position z is expressed as:

$$\sigma = \rho g \left(z - \frac{1}{3} r \right) \tag{10}$$

According to the Tresca yield criterion, the maximum shear stress is numerically equal to one-half of the stress:

$$\sigma_{Max} = \frac{1}{2} \sigma = \frac{1}{2} \rho g \left(z - \frac{1}{3} r \right) \tag{11}$$

The LMTA is an incompressible fluid, so the volume of the integral unit remains unchanged before and after the slump:

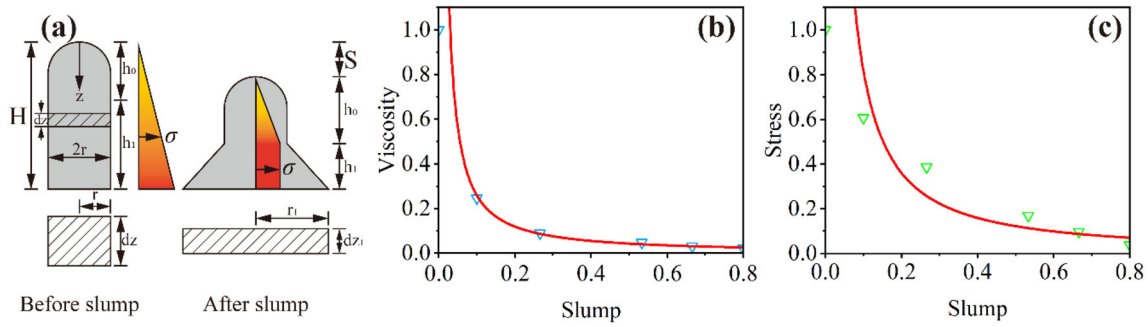


Fig. 8 a Schematic diagram of mini-slump method; b Relationship between viscosity and slump; c Relationship between yield stress and slump

$$\pi r^2 dz = \pi r_1^2 dz_1 \tag{12}$$

After transforming Formula (12), we can obtain:

$$dz_1 = \left(\frac{r}{r_1}\right)^2 dz \tag{13}$$

Where r_1 is the radius of the cylinder after the slump. Assuming there is no flow between the inner layers of the composites, the shear stress increases within the range of h_0 until it equals to the yield stress. This relationship can be expressed as:

$$\sigma \pi r^2 = \sigma_1 \pi r_1^2 = \sigma_0 \pi r_1^2 \tag{14}$$

So,

$$\left(\frac{r}{r_1}\right)^2 = \frac{\sigma_0}{\sigma} \tag{15}$$

The deformation region h_1 can be expressed as:

$$h_1 = \int_{h_0}^H dz_1 \tag{16}$$

Substitute Formula (13) and (15) into Formula (16) and integrate:

$$h_1 = \frac{2\sigma_0}{\rho g} \ln \frac{\rho g (H - \frac{1}{3}r)}{2\sigma_0} \tag{17}$$

The stress at h_0 can be expressed as:

$$\sigma_0 = \frac{1}{2} \rho g \left(h_0 - \frac{1}{3}r\right) \tag{18}$$

Therefore, h_0 can be written as:

$$h_0 = \frac{2\sigma_0}{\rho g} + \frac{1}{3}r \tag{19}$$

As shown in Fig. 7a, slump $S = H - h_0 - h_1$. Therefore, the relationship between slump S and yield stress σ_0 can be expressed as

$$S = H - \frac{\sigma_0}{\rho g} - \frac{1}{3}r + \frac{2\sigma_0}{\rho g} \ln \frac{2\sigma_0}{\rho g (H - \frac{1}{3}r)} \tag{20}$$

Where $H = 0.015$ m, $r = 0.0035$ m.

The viscosity η can be determined according to Arrhenius type empirical equation [40] and Thomas’s [41] viscosity model.

$$\eta' = \eta_0 \exp\left(\frac{E}{RT}\right) \tag{21}$$

$$\eta = \eta' [1 + 2.5\Phi + 10.05\Phi^2 + A \exp(B\Phi)] \tag{22}$$

Where η' is the viscosity of LMTA at 298 K, $E = 3904$ J/mol is the fit parameter, $R = 8.3144$ J/mol·K is the gas constant, T is the absolute temperature (K), $\eta_0 = 0.4352$ mPa·s. For this expression, coefficients A and B are 0.00273 and 16.6, respectively.

Through dimensionless treatment of viscosity η , yield stress σ_0 and slump S , the following equation can be obtained:

$$\eta = \frac{0.02}{S^{1.12}} \tag{23}$$

$$\sigma_0 = \frac{0.05}{S^{1.18}} \tag{24}$$

It can be seen that viscosity η , yield stress σ_0 , and slump S are nonlinear negatively correlated, as shown in Fig. 8b and c.

The slump of LMTA/CCDP composite TIMs as a function of the CCDP mixing volume ratio is shown in Fig. 9a. As the CCDP mixing volume ratio increased from 10 to 60%, the slump sharply decreases from 12 to 0 mm. When the CCDP mixing volume ratio exceeds 60%, the composite will not collapse, indicating that there is no flow without external force. According to formula (20) and (22), the functional relationship between stress and shear rate

is shown in Fig. 9b. There is a linear relationship between stress and shear rate: intercept represents yield stress σ_0 and slope represents viscosity η . It can be seen that as the CCDP mixing volume ratio increases from 10 to 60%, the intercept and slope of the function gradually increase, which means that the yield stress and viscosity gradually increase.

With the increase of the CCDP mixing volume ratio, there are four states of the liquid phase in the LMTA/CCDP composite TIMs: immersed state, capillary state, chain state, and swing state, as shown in Fig. 9c. In the immersed state, CCDPs are completely immersed in the LMTA. In the capillary state, the pores between CCDPs are filled with LMTA, forming a gas–liquid–solid three-phase interface on the diamond surface. In the chain state, only part of the pores between CCDPs are filled with LMTA, the liquid phase in the pores connects with CCDPs to form a chain-like state. In the swing state, CCDPs are coated with LMTA, and connected by a biconcave lens shape liquid bridge. It is precisely because of this change related to the internal state of the LMTA/CCDP composite TIMs that its liquidity shows a trend as shown in Fig. 9a.

The viscosity of the LMTA/CCDP composite TIMs showed a gradual upward trend with the increase of

CCDP content, and when the CCDP mixing volume ratio exceeded 50%, the viscosity increased sharply, as shown in Fig. 9d. There are two main reasons for this phenomenon. First, pure liquid metal is regarded as a non-Newtonian fluid and flows in laminar flow. With the increase of diamond content, the laminar flow state of liquid metal is gradually disordered, increasing the viscosity of the LMTA/CCDP composite TIMs. Secondly, the increase in diamond content leads to a decrease in liquid metal content, leads to changes in the internal structure of LMTA/CCDP composite TIMs. The liquid metal inside the LMTA/CCDP composite TIM is divided into two parts, one for coating diamonds, and the other for filling the pores between diamonds. The reduction in liquid metal content directly leads to the inability of the pores between diamonds to be filled, resulting in a less liquid metal that can flow, causing an increase in viscosity.

Furthermore, the specific viscosity in Fig. 9d also reveals that the increase in CCDP content is the main reason for the increase in viscosity of LMTA/CCDP composite TIMs. The specific viscosity is defined as:

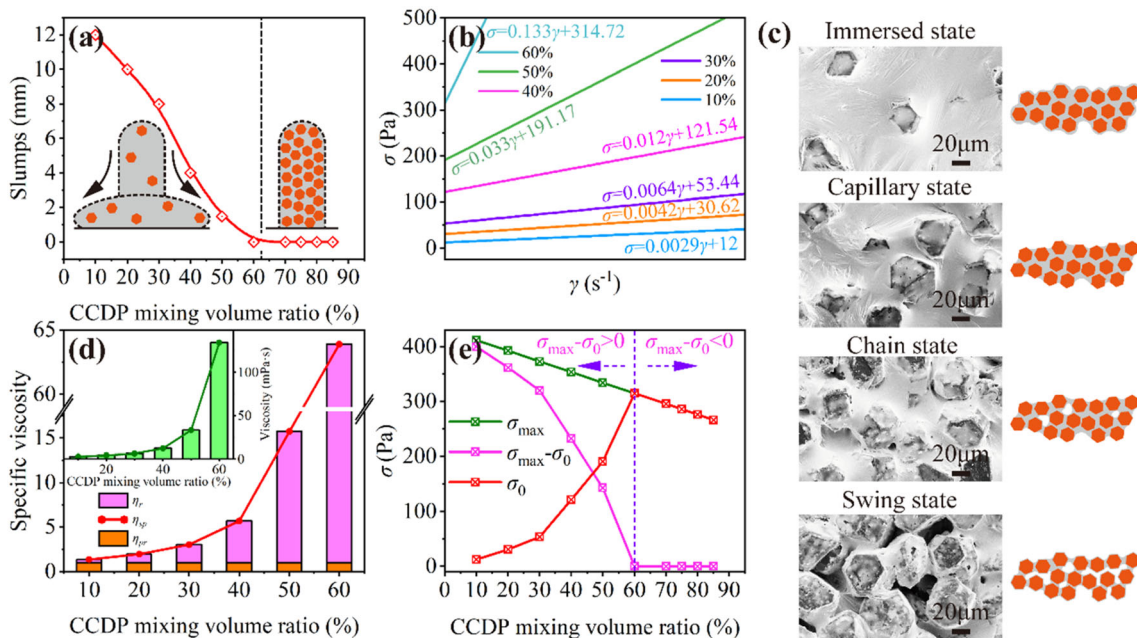


Fig. 9 a Slump of LMTA/CCDP composite TIMs in the different volume mixing; b Rheological characteristic curve of LMTA/CCDP composite TIMs with CCDP mixing volume ratio from 10–60%; c Four kinds of the static liquid phase in LMTA/CCDP

composite TIMs; d Viscosity and specific viscosity change with CCDP mixing volume ratio; e Maximum stress and yield stress with CCDP mixing volume ratio

$$\eta_r = \frac{\eta}{\eta'} \quad (25)$$

$$\eta_{sp} = \frac{\eta - \eta'}{\eta'} = \frac{\eta}{\eta'} - 1 = \eta_r - 1 \quad (26)$$

Where η_r and η_{sp} are the relative viscosity and specific viscosity of the LMTA/CCDP composite TIMs, respectively. η_{pr} is the relative viscosity of pure LMTA. The specific viscosity has deducted the effect of internal friction effect of pure LMTA. When the CCDP mixing volume ratio is 10%, the η_{pr} is greater than the η_{sp} , indicating that the viscosity of the LMTA/CCDP composite TIM depends on the internal friction behavior of pure LMTA. When the CCDP mixing volume ratio is 20%, the η_{sp} is close to the η_{pr} , indicating that the viscosity of the LMTA/CCDP composite TIM is influenced by the common effect of CCDP and LMTA. However, when the CCDP mixing volume ratio exceeds 30%, the η_{sp} is much larger than the η_{pr} , and the internal friction effect of pure LMTA can be ignored at this time. The viscosity of the LMTA/CCDP composite TIMs is mainly determined by the interaction between CCDPs.

The curves of maximum stress σ_{Max} , yield stress σ_0 and the differential value of maximum stress and yield stress $\sigma_{Max} - \sigma_0$ with CCDP mixing volume ratio are shown in Fig. 9e. The maximum stress σ_{Max} decreases with the increase of the CCDP mixing volume ratio. Because the density of CCDP is smaller than that of LMTA, the increase of the CCDP mixing volume ratio leads to a decrease in the density of LMTA/CCDP composite TIMs. According to formula (11), the maximum stress is related to the density and shows a downward trend. Taking the CCDP mixing volume ratio of 60% as the threshold, the yield stress σ_0 is divided into two stages. When the CCDP mixing volume ratio is less than 60%, the yield stress increases with the increase of the CCDP mixing volume ratio, and when the CCDP mixing volume ratio is more than 60%, the yield stress decreases with the increase of the CCDP mixing volume ratio. The formula (21) shows that the yield stress is related to the slump and density. When the CCDP mixing volume ratio is less than 60%, the yield stress is mainly affected by the slump. The differential value of maximum stress and yield stress $\sigma_{Max} - \sigma_0 > 0$, indicates that the maximum stress is greater than the yield stress, and the LMTA/CCDP composite TIMs material slump and deform. When the CCDP mixing

volume ratio is more than 60%, the slump is no longer changed, the yield stress is mainly affected by the density of the LMTA/CCDP composite TIMs. The differential value of maximum stress and yield stress $\sigma_{Max} - \sigma_0 < 0$, indicates that the yield stress is greater than the maximum stress, and the LMTA/CCDP composite TIMs do not deform. Whether or not the LMTA/CCDP composite TIMs deform depends on the difference between the maximum stress and the yield stress. With the increase of the CCDP mixing volume ratio, the difference between the maximum stress and the yield stress decreases rapidly, indicating that the deformation resistance of the LMTA/CCDP composite TIMs increases, thus the slump gradually decreases until the CCDP mixing volume ratio exceeds 60%.

The flowability of LMTA/CCDP composite TIMs is also related to the formation of liquid bridges in addition to changes in stress and viscosity. After the CCDP is mixed with LMTA, a layer of the LMTA coated on the CCDP surface, as shown in Fig. 10a. During the pressing process, the LMTA on the particle surface gradually contacts and fuses, forming a liquid bridge with a biconcave lens shape. Due to the existence of surface tension and capillary pressure difference, there is an interaction force between particles, called capillary force. The simplified model is shown in Fig. 10b. According to the Young–Laplace equation, the capillary force pressures difference Δp is.

$$\Delta p = \tau \left(\frac{1}{R_1} - \frac{1}{R_2} \right) \quad (27)$$

Where τ is the surface tension of LMTA, R_1 and R_2 are the curvature radius of the liquid bridge. According to the theory of Fisher [42], the capillary force F between particles can be obtained:

$$F = 2\pi R_2 \tau + \pi R_2^2 \tau \left(\frac{1}{R_1} - \frac{1}{R_2} \right) \quad (28)$$

At the same time, according to geometry, the following relationship can be derived:

$$R_1 = \frac{a(1 - \cos \theta) + \frac{D}{2}}{\cos \theta} \quad (29)$$

$$R_2 = a \sin \theta + R_1(\sin \theta - 1) \quad (30)$$

Where a is the radius of a spherical particle, D is the distance between spherical particle surfaces, and θ is the liquid angle. In this study, the diameter of CCDPs

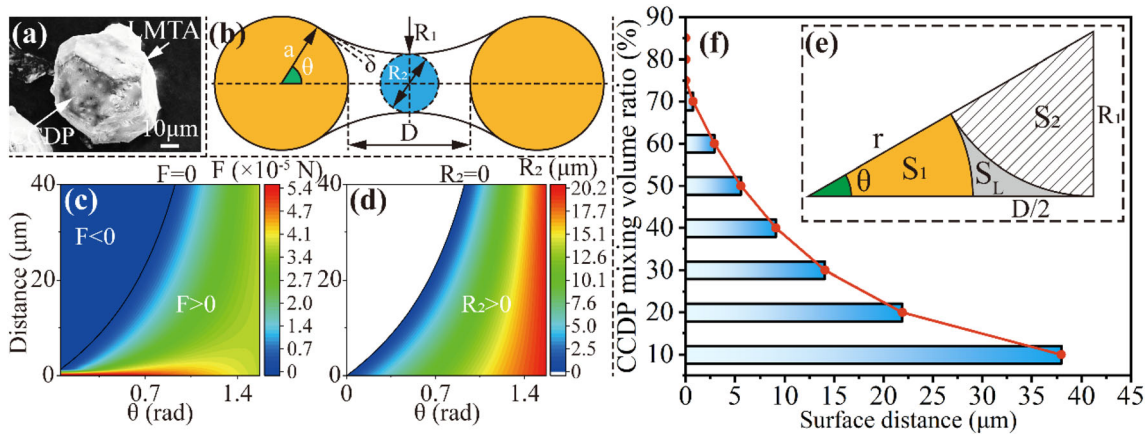


Fig. 10 Effect of the surface distance of particles on liquid bridge formation. **a** Microstructure of CCDP is coated by LMTA; **b** Liquid bridge with biconcave lens shape two spheroidal particles; **c** Variation trend of intergranular capillary force with the surface distance of particles and liquid angle θ ; **d** Variation

trend of R_2 with the surface distance of particles and liquid angle θ ; **e** Diagram of the minimum volume of the liquid bridge; **f** Variation trend of the surface distance of particles with CCDP mixing volume ratio in sphere model close packing

is about 40 μm , the surface tension of LMTA is about 585 $\text{m}\cdot\text{N}/\text{m}$ [40], and the wetting angle between LMTA and particles is 0. After substituting the above values into formulas (28), (29), and (30), the function images of capillary force F and curvature radius R_2 concerning the surface distance D of spherical particles and liquid angle θ can be obtained, as shown in Fig. 10c and d. It is clearly that F is more sensitive to the change in D , while R is more sensitive to the change in θ .

When $R_2 = 0$, the liquid bridge reaches the critical state of impending fracture. Therefore, according to the geometric relation, the area of the triangle and sector can be expressed as:

$$S_{\text{triangle}} = \frac{R_1}{2} \left(\frac{D}{2} + a \right) \tag{31}$$

$$S_1 = \frac{\theta\pi a}{180} \tag{32}$$

$$S_2 = \frac{(90 - \theta)\pi R_1}{180} \tag{33}$$

So, $S_{\text{triangle}} - S_1 - S_2$ is the cross-sectional area of the liquid bridge S_L :

$$S_L = \frac{R_1}{2} \left(\frac{D}{2} + a \right) - \left[\frac{\pi R_1}{2} - \frac{\theta\pi}{180} (R_1 - a) \right] \tag{34}$$

According to formula (34) and Fig. 10e, when $R_1 = a$, the cross-sectional area of the liquid bridge is the smallest, that is, the volume of the liquid bridge is the smallest. By calculating, the liquid angle θ and the particle surface distance D at this time is 30 degrees and 29.28 μm , respectively. This indicates that when the mixing volume ratio of CCDP exceeds 10%, the liquid bridge gradually formed, as shown in Fig. 10e. The formation of liquid bridges in the LMTA/CCDP composite TIM helps to improve the bonding between CCDPs, thereby increasing the viscosity of the LMTA/CCDP composite TIMs.

Compared with common LMTA TIMs, the LMTA/CCDP composite TIM shows significantly higher thermal conductivity and viscosity, as shown in Fig. 11a. When the LMTA/CCDP composite TIM with 50% CCDP contents was applied to a vertically placed glass sheet, it was found that the TIM was easy to adhere to the smooth glass surfaces without peeling, and had good wettability, as shown in Fig. 11b1 and b2. In addition, the LMTA/CCDP composite TIM can easily spread on the surface of the glass sheet after applying slight pressure on the sample, as shown in Fig. 11b3. Therefore, the LMTA/CCDP composite TIM can simultaneously meet the requirements of higher thermal conductivity and low flowability, becoming an advantageous alternative for thermal interface materials.

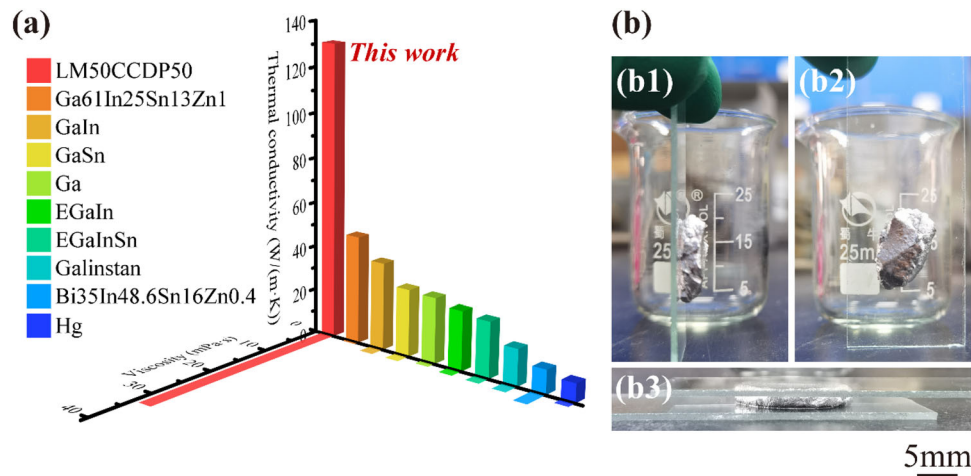


Fig. 11 **a** Viscosity of commercial TIMs and this work; **b** Flowability of composites at 50% CCDP content: **b1** and **b2** The composite material was placed on a glass plate and then the plate was stood up to observe the adhesion of the composite to

the smooth glass plate; **b3** Positive pressure is applied to a composite material resting on a glass plate to observe the deformation of the composite material

Table 2 Density of LMTA/CCDPs composite TIMs with CCDP mixing volume ratio

LMTA: CCDP	100:0	90:10	80:20	70:30	60:40	50:50	40:60
Density (g/cm ³)	6.36	6.07	5.79	5.50	5.22	4.93	4.64

4 Conclusions

The effect of CCDP mixing volume ratio on the thermal conductivity and flowability of LMTA/CCDP composite TIMs were investigated in this paper. The following main conclusions were drawn:

1. The thermal conductivity of the LMTA/CCDP composite TIMs increases first and then decreases with the increase of CCDP mixing volume ratio, showing a bell-shaped trend. When the ratio of LMTA to CCDP is 1:1, the thermal conductivity of the LMTA/CCDP composite TIM reaches a peak of 126 ± 6 W/m·K.
2. The distance between CCDPs in LMTA has an important influence on the thermal transfer performance of the LMTA/CCDP composite TIMs. When the CCDPs content is less than 30%, the particles are uniformly dispersed in the matrix, and the thermal conductivity of TIM conforms to the DEM model. But when the CCDP content reaches 40%, the CCDPs formed a chain-like structure connected by LMTA, greatly enhancing heat transfer. With the further increase of CCDPs content, the gradually increasing pores have a destructive effect on the heat transfer structure,

and the heat transfer performance gradually deteriorates.

3. The flowability of LMTA/CCDP composite TIMs shows a decreasing trend with the increase of diamond content. When the ratio of diamond to liquid metal is 1:1, the LMTA/CCDP composite TIM is in a paste state, and the flowability of the LMTA is effectively controlled.
4. When the CCDP content exceeds 30%, LMTA liquid bridges were formed between CCDPs. The capillary force accompanying the formation of the liquid bridge effectively restricts the motion behavior between diamonds and has a positive impact on reducing the overall flowability of LMTA/CCDP composite TIMs.

Acknowledgements

This work was supported by the National Natural Science Foundation of China (Grant No. 51971231), Guangxi Natural Science Foundation (Grant No. 2020GXNSFBA297109), Guangxi Science and Technology Program (Grant No. Guike AD20297023), and

Science and Technology Plan Project of Yunnan province (Grant No. 202101BC070001-007).

Author contributions

Conceptualization: WW, JG; Data curation: WW, XD, ZD; Formal analysis: WW, SW; Investigation: WW, XD, ZD; Validation: WW; Writing—Original Draft: WW; Writing—Review & Editing: WW, SW, JG; Methodology: SW; Resources: QZ, YQ, XW, JG; Funding acquisition: JG; Project administration: JG; Supervision: JG.

Funding

This study was funded by National Natural Science Foundation of China (51971231); Guangxi Science and Technology Program (2020GXNSFBA297109); - Guangxi Science and Technology Program (Guike AD20297023); Science and Technology Plan Project of Yunnan province (202101BC070001-007).

Data availability

All data supporting the conclusions of this study are included in the article.

Declarations

Conflict of interest The authors declare that they have no known competing financial interests or personal relationships that could have appeared to influence the work reported in this paper.

References

1. G. Becker, C. Lee, Z. Lin, *Adv. Pack.* **14**, 1 (2005)
2. R. Viswanath, V. Wakharkar, A. Watwe, V. Lebonheur, *Intel. Technol. J.* **4**, 1 (2000)
3. Y. Deng, Y. Jiang, *Appl. Therm. Eng.* **199**, 1 (2021)
4. X. Guo, S. Cheng, W. Cai, Y. Zhang, X.- Zhang, *Mater. Des.* **209**, 1 (2021)
5. M. Mozafari, A. Lee, J. Mohammadpour, *Therm. Sci. Eng. Prog.* **23**, 1 (2021)
6. R. Septimio, C. Cruz, M. Xavier, T. Lima, A. Garcia, J.E. Spinelli, N. Cheung, *Int. J. Therm. Sci.* **160**, 1 (2021)
7. X. Wang, C. Lu, W. Rao, *Appl. Therm. Eng.* **192**, 1 (2021)
8. S. Chen, H.-Z. Wang, R.-Q. Zhao, W. Rao, J. Liu, *Matter* **2**, 1446–1480 (2020)
9. Y.X. Gao, J. Liu, X.P. Wang, Q.F. Fang, *J. Eng. Thermophys.* **38**, 1077–1081 (2017)
10. Y. Martin, T. Kessel, in: IMAPS 40th international symposium on microelectronics, San Jose, CA(US), 2007, pp. 1–7
11. K. Huang, W. Qiu, M. Ou, X. Liu, Z. Liao, S. Chu, *RSC Adv.* **10**, 18824–18829 (2020)
12. C.K. Roy, S. Bhavnani, M.C. Hamilton, R.W. Johnson, J.L. Nguyen, R.W. Knight, D.K. Harris, *Int. J. Heat. Mass. Transf.* **85**, 996–1002 (2015)
13. C.K. Roy, S. Bhavnani, M.C. Hamilton, R.W. Johnson, R.W. Knight, D.K. Harris, *Microelectron. Reliab.* **55**, 2698–2704 (2015)
14. C.K. Roy, S. Bhavnani, M.C. Hamilton, R.W. Johnson, R.W. Knight, D.K. Harris, *Appl. Therm. Eng.* **99**, 72–79 (2016)
15. R.F. Hill, J.L. Strader, in: 22nd annual IEEE semiconductor thermal measurement and management symposium, Ieee, Dallas, TX, 2006, pp. 23
16. J. Tang, X. Zhao, J. Li, R. Guo, Y. Zhou, J. Liu, *ACS Appl. Mater. Interfaces.* **9**, 35977–35987 (2017)
17. S. Ki, J. Shim, S. Oh, E. Koh, D. Seo, S. Ryu, J. Kim, Y. Nam, *Int. J. Heat. Mass. Transf.* **170**, 1 (2021)
18. J. Liu, U. Sahaym, I. Dutta, R. Raj, M. Renavikar, R.S. Sidhu, R. Mahajan, *J. Mater. Sci.* **49**, 7844–7854 (2014)
19. Z. Lin, H. Liu, Q. Li, H. Liu, S. Chu, Y. Yang, G. Chu, *Appl. Phys. A* **124**, 1 (2018)
20. B.L. Silva, A. Garcia, J.E. Spinelli, *Mater. Charact.* **114**, 30–42 (2016)
21. W. Kong, Z. Wang, M. Wang, K.C. Manning, A. Uppal, M.D. Green, R.Y. Wang, K. Rykaczewski, *Adv. Mater.* **31**, e1904309 (2019)
22. A.C. I, A.F. Chrimes, A. Zavabeti, K.J. Berean, B.J. Carey, J. Zhuang, Y. Du, S.X. Dou, K. Suzuki, R.A. Shanks, R. Nixon-Luke, G. Bryant, K. Khoshmanesh, K. Kalantar-Zadeh, T. Daeneke, *Nano Lett.* **17**, 7831–7838 (2017)
23. X. Wang, W. Yao, R. Guo, X. Yang, J. Tang, J. Zhang, W. Gao, V. Timchenko, J. Liu, *Adv. Healthc. Mater.* **7**, e1800318 (2018)
24. M. Ralphs, W. Kong, R.Y. Wang, K. Rykaczewski, *Adv. Mater. Interfaces* **6**, 1 (2019)
25. S. Wei, Z.F. Yu, L.J. Zhou, J.D. Guo, *J. Mater. Sci.: Mater. Electron.* **30**, 7194–7202 (2019)
26. C. Zeng, J. Shen, J. Zhang, *Diam. Relat. Mater.* **112**, 1 (2021)
27. C. Zeng, J. Shen, C. He, H. Chen, *Scr. Metall.* **170**, 140–144 (2019)
28. S. Arai, M. Ueda, *J. Appl. Electrochem.* **50**, 631–638 (2020)
29. L. Han, L. Huiqiang, L. Zuoye, C. Sheng, *Rare Met. Mater. Eng.* **47**, 2668–2674 (2018)

30. W. Kong, Z. Wang, N. Casey, M.M. Korah, A. Uppal, M.D. Green, K. Rykaczewski, R.Y. Wang, *Adv. Mater. Interfaces* **8**, 1 (2021)
31. H. Chang, P. Zhang, R. Guo, Y. Cui, Y. Hou, Z. Sun, W. Rao, *ACS Appl. Mater. Interfaces*. **12**, 14125–14135 (2020)
32. Z. Ji, W. Liu, C. Ouyang, Y. Li, *Mater. Adv.* **2**, 5977–5985 (2021)
33. X. Ge, J. Zhang, G. Zhang, W. Liang, J. Lu, J. Ge, *ACS Appl. Nano Mater.* **3**, 3494–3502 (2020)
34. L. Zhao, S. Chu, X. Chen, G. Chu, *Bull. Mater. Sci.* **42**, 1 (2019)
35. Y. Ji, G. Li, C. Chang, Y. Sun, H. Ma, *J. Heat. Transf.* **137**, 1 (2015)
36. C. Wang, Y. Gong, B.V. Cunning, S. Lee, Q. Le, S.R. Joshi, O. Buyukcakir, H. Zhang, W.K. Seong, M. Huang, M. Wang, J. Lee, G.H. Kim, R.S. Ruoff, *Sci. Adv.* **7**, 3767 (2021)
37. G. Li, Y. Ji, Q. Zhang, B. Tian, H. Ma, *J. Heat. Transf.* **138**, 8 (2016)
38. Y. Yamamoto, T. Imai, K. Tanabe, T. Tsuno, Y. Kumazawa, N. Fujimori, *Diam. Relat. Mater.* **6**, 1057–1061 (1997)
39. A.G. Every, Y. Tzou, D.P.H. Hasselman, R. Raj, *Acta Metall. Mater.* **40**, 123–129 (1992)
40. Y. Plevachuk, V. Sklyarchuk, S. Eckert, G. Gerbeth, R. Novakovic, *J. Chem. Eng. Data.* **59**, 757–763 (2014)
41. D.G. Thomas, *J. Colloid Sci.* **20**, 267–277 (1965)
42. R.A. Fisher, *J. Agric. Sci.* **16**, 492–505 (2009)

Publisher's Note Springer Nature remains neutral with regard to jurisdictional claims in published maps and institutional affiliations.

Springer Nature or its licensor (e.g. a society or other partner) holds exclusive rights to this article under a publishing agreement with the author(s) or other rightsholder(s); author self-archiving of the accepted manuscript version of this article is solely governed by the terms of such publishing agreement and applicable law.